Nationaal Lucht- en Ruimtevaartlaboratorium
National Aerospace Laboratory NLR

NLR-TP-2000-051

Accurate and efficient vortex-capturing for rotor blade vortex interaction

O.J. Boelens, H. van der Ven, B.Oskam and A.A. Hassan

Nationaal Lucht- en Ruimtevaartlaboratorium
National Aerospace Laboratory NLR

NLR-TP-2000-051

Accurate and efficient vortex-capturing for rotor blade vortex interaction

O.J. Boelens, H. van der Ven, B.Oskam and A.A. Hassan*

* *The Boeing Company, Mesa*

This report has been presented as AIAA paper 2000-0112 at the 38th American Institute of Aeronautics and Astronautics Aerospace Sciences Meeting and Exhibit, January 10-13, 2000, Reno (NV), U.S.A.
The Boeing Company (Mesa) has granted NLR permission to publish this report.

Division:	Fluid Dynamics
Issued:	February 2000
Classification of title:	unclassified

Title : Accurate and Efficient Vortex-Capturing for Rotor Blade-Vortex Interaction
Author(s) : O.J. Boelens, H. van der Ven, B. Oskam and A.A. Hassan
date : 02-02-2000

Executive summary

The objective of this paper is to present an innovative CFD algorithm for the simulation of wake vortices generated by helicopter rotors. Special emphasis is placed on the CFD technology in terms of:

- basic requirements for these CFD algorithms,
- general CFD development stages,
- important CFD issues such as accuracy, efficiency and parallelization, and
- demonstration of a prototype CFD system on test cases relevant for vortex wake simulation.

The CFD algorithm presented is characterized by the following key components:

- the conservation laws are formulated in an Arbitrary Lagrangian Eulerian (ALE) framework using a single, dynamically deforming and boundary conforming, hexahedral grid,
- the conservation laws are discretized using a second-order accurate discontinuous Galerkin finite element method,
- the boundary conforming, hexahedral grid is adaptively refined and derefined on an element-by-element basis depending upon a vorticity sensor.

This algorithmic CFD research falls under the proliferation stage of CFD development. One of the conclusions of this CFD research is that the proposed, innovative CFD algorithm which combines the standard ALE formulation with the unconventional DG finite element method (including grid adaption) can meet the basic requirements for CFD algorithms that need to be satisfied if one wishes to establish standard and reliable CFD tools for BVI noise.

This report has been presented as AIAA paper 2000-0112 at the 38^{th} American Institute of Aeronautics and Astronautics Aerospace Sciences Meeting & Exhibit, January 10-13, 2000, Reno, NV, USA.

Contents

List of figures 6

1 Introduction 9
- 1.1 Blade-vortex interaction background 9
- 1.2 BVI prediction 9
- 1.3 Basic requirements for CFD algorithms 10
- 1.4 CFD development stages 10
- 1.5 Outline of paper 11

2 CFD algorithm 12
- 2.1 Discontinuous Galerkin method 12
- 2.2 Unique features 12
- 2.3 Standard features 12
- 2.4 Vortex sensor and vortex grid adaption 13

3 Extensions for rotor simulations 14
- 3.1 Blade motion definition 14
- 3.2 Grid deformation algorithm 14
- 3.3 Boundary conditions for rotor in hover 14
- 3.4 Rotor in hover as steady state problem 15
- 3.5 Rotary stagnation pressure 15

4 Accuracy and efficiency 16

5 Transonic unsteady rotor Navier-Stokes(TURNS) 17

6 Test cases 18

7 ONERA M6 results 19
- 7.1 Fine grid 19
- 7.2 Grid adaption 19
- 7.3 Need for extension to Navier-Stokes 20

8 Caradonna-Tung rotor in hover 21

8.1 Caradonna-Tung OH-grid 21

8.2 Caradonna-Tung multi-block grid 21

8.3 Caradonna-Tung CH-grid 22

8.4 Caradonna-Tung surface pressure results 22

8.5 Vortex persistence for Caradonna-Tung rotor 22

9 Discussion 24

10 Concluding remarks 25

(39 pages in total)

List of figures

Figure 1 Convergence of the residuals for the ONERA M6 simulation on the fine grid (440,320 elements) ($\alpha = 6°$ and $M_\infty = 0.4$). 30

Figure 2 Iso-contour of the total pressure loss (0.01) for the ONERA M6 simulation on the fine grid (440,320 elements) ($\alpha = 6°$ and $M_\infty = 0.4$), demonstrating DG capability to accurately simulate the persistence of the trailing vorticity. 31

Figure 3 The relative vortex strength, i.e. vortex strength/vortex strength at one wing span, for the ONERA M6 wing ($\alpha = 6°$ and $M_\infty = 0.4$). Both the relative vortex strength based on the total pressure loss and the vortex strength are shown. 31

Figure 4 The Caradonna-Tung grid near the blade (726,784 elements): (a) the blade and the plane trough the leading edge, trailing edge and blade tip, (b) the blade and a grid plane perpendicular to the blade. The rotor blade is coloured grey. The block boundaries are coloured red. 32

Figure 5 The upper part of the Caradonna-Tung grid (726,784 elements): (a) the complete grid, (b) detail near the rotor blade. The rotor blade is coloured grey. The block boundaries are coloured red. 33

Figure 6 The lower part of the Caradonna-Tung grid (726,784 elements): (a) the complete grid, (b) detail near the rotor blade. The rotor blade is coloured grey. The block boundaries are coloured red. 34

Figure 7 Comparison of -C_p-distribution for the Caradonna-Tung helicopter rotor in hover (collective pitch: 12°, $M_{tip} = 0.61$, $Re = 2.7 \cdot 10^6$): C_T=0.0094 on the fine grid. 35

Figure 8 Rotary stagnation pressure loss contours at different radial cross-section for the Caradonna-Tung helicopter rotor in hover on the medium adapted grid (a) and on the fine grid (b) (collective pitch: 12°, $M_{tip} = 0.61$). 36

Figure 9 The adapted Caradonna-Tung grid (135,280 elements). Shown are the periodic plane at z=0 and the plane at x=-3.6. 37

Figure 10 Iso-contour of the rotary stagnation pressure loss for the Caradonna-Tung helicopter rotor in hover on the medium adapted grid (a) and on the fine grid (b) (collective pitch: 12°, $M_{tip} = 0.61$). 38

Figure 11 Iso-contour of the rotary stagnation pressure loss near the tip for the Caradonna-Tung helicopter rotor in hover on the fine grid. (collective pitch: 12°, $M_{tip} = 0.61$). 39

Nomenclature

Symbols

a_∞	Freestream speed of sound
c	Chord length
C_p	Pressure coefficient
H_r	Rothalpy
M_∞	Freestream Mach number
$M_{tip} = \Omega R_{tip}/a_\infty$	Tip Mach number
p	Pressure (scaled with $\rho_\infty a_\infty^2$; $p_\infty = 1/\gamma$)
P_{rs}	Rotary stagnation pressure loss
R, R_{tip}	Rotor blade tip radius
Re	Reynolds number
$\mathbf{s}$	Grid velocity vector (scaled with a_∞)
$\mathbf{u}$	Velocity vector (scaled with a_∞); $\mathbf{u}_\infty = \mathbf{0}$)
u, v, w	Velocity components in x, y, z-direction (scaled with a_∞)
x, y, z	Coordinate directions (scaled with c)

Greek symbols

α	Pitching angle
γ	Ratio of specific heats
ξ, η, ζ	Coordinate directions in computational space
ρ	Density (scaled with ρ_∞)
ρ_∞	Freestream density
ω	Vorticity ($\nabla \times \mathbf{u}$)
Ω	Angular frequency of rotor [rpm]

This page is intentionally left blank.

1 Introduction

1.1 Blade-vortex interaction background

The aerodynamics and acoustics of blade-vortex interaction have been extensively studied in several large experimental programs, i.e. the OLS program (Refs. 5, 18, 31), the AATMR program (Ref. 14), the HART program (Refs. 20, 25) and the HELINOISE program (Ref. 19). These experimental programs, which were conducted in the German-Dutch Wind Tunnel (DNW), have provided a large set of aerodynamic and acoustic data, which has shed more light on a number of key parameters associated with complex blade-vortex interactions. It is nevertheless concluded from the HART program (Ref. 20) that more specific information, e.g. the vortex roll-up, the streamwise convection, the vortex aging from tip emission to blade encounter and eventually the vortex bursting, are required to completely understand the physics of blade-vortex interaction (BVI).

BVI's are caused by the close encounters between rotor blades and tip vortices shed from the preceding blades or even the same blade. Strong interactions which result in large chordwise temporal pressure variations are caused by a vortex whose axis is parallel (or nearly parallel) to the spanwise axis of the blade (Ref. 10). Blade-vortex interactions predominantly occur in low-speed descent flight where the vortex wake remains near the rotor disk. However, they can also occur during maneuvers and in forward flight for tandem rotor helicopters.

Blade-vortex interactions take place on both the advancing and the retreating sides of the rotor disk. However, from an acoustics point of view, the interactions on the advancing side are more dominant due to the locally higher Mach numbers.

1.2 BVI prediction

The presently available solution techniques for predicting the unsteady aerodynamic response of rotor blades during BVI can be classified in two categories:

(i) vortex based methods, with a rigidly prescribed wake geometry or with a free wake geometry, and

(ii) Euler/Navier-Stokes methods.

Vortex based methods have more severe limitations than the more comprehensive Euler/Navier-Stokes methods. Some of the deficiencies of vortex based methods are well known and are related to the additional unknown parameters (core size parameters), which have a direct influence on the position and/or motion of the vortex.

To accurately predict blade-vortex interaction noise, one must accurately compute the location as well as the strength of the tip vortex wake from the CFD model itself since small changes in these parameters can result in significant differences in the blade-vortex interaction noise levels.

In recent years there has also been a large body of research in helicopter aerodynamics aimed at applying and/or improving Euler/Navier-Stokes CFD techniques originally developed for fixed wing aircraft (Ref. 10). The two techniques commonly used are the 'Chimera' or Overset grid technique (Refs. 3, 12, 22, 30, 24, 13) and the more recent methods based on the Arbitrary Lagrangian Eulerian (ALE) approach using a dynamically deforming, boundary conforming grid (Refs. 4, 29). Despite all this CFD research, experimental programs are the dominant approach in industrial projects.

1.3 Basic requirements for CFD algorithms

The following basic requirements are identified as important issues to be considered during the present study:

(i) The CFD algorithm should allow for a realistic simulation of rotor wakes with the object of predicting BVI noise. Realistic means that the CFD algorithm is required to handle general blade motion. The blade motion functionality represents the helicopter blade pitch, flap and lead-lag motions, and elastic deformations.

(ii) The CFD algorithm should be able to accurately capture tip vortices over a distance of one-and-a-half revolutions to enable BVI.

(iii) Since the simulations are time-dependent with a long transient the CFD algorithm must be computationally efficient for the computing times to be reasonable.

Over the past years, NLR has developed an ALE formulation in conjunction with a grid adaption technique based on anisotropic refinement of hexahedral elements (Ref. 26). This method, though developed for fixed wing aircraft applications, provides a number of key technologies enabling accurate simulations of helicopter rotor blade-vortex interactions.

Exploring the applicability of these unconventional CFD technologies to rotor wake problems requires a long term point of view. For that reason it is important to recognise the various CFD development stages.

1.4 CFD development stages

Within the Boeing Company four stages are identified in the development of CFD capabilities. These stages are in chronological order (Ref. 9):

(i) the discussion stage, which incorporates the identification of the specific CFD need, the consideration of the objectives and approaches and a research on the feasibility,

(ii) the proliferation stage, where attention is focussed on the technology, important issues of the problem are explored, prototype systems using various approaches are built and initial applications are demonstrated,

(iii) the standards stage, in which consensus on the objectives and approaches has to be achieved and attention focusses on interoperability, robustness, metrics, etc. and

(iv) the reliance stage, where attention is focussed on the processes and not the technology, the emphasis lies on consistent and assured quality, high throughput, user support and embedding the CFD capability in large processes.

The algorithmic research of this paper falls in the proliferation stage of CFD development.

1.5 Outline of paper

First the discontinuous Galerkin (DG) finite element method is outlined. Special attention is paid to the vortex sensor and vortex grid adaption. Some of the extensions applied to the DG method to be able to simulate the flow field for a helicopter rotor in hover or in forward flight are discussed next. Important issues of the rotor problem are the blade motion, the grid deformation, the boundary conditions for a helicopter rotor in hover, the definition of a rotor in hover as a steady state problem, the accuracy and efficiency of the flow solver and the vortex sensor. In addition the rotary stagnation pressure loss is introduced. The vortex grid adaption sensor is demonstrated by simulations on the ONERA M6 wing. The capabilities of the flow solver in simulating the flow field of a hovering rotor are demonstrated by simulations for the Caradonna-Tung rotor. A new grid around the Caradonna-Tung rotor is generated. A complete section is dedicated to the description of this grid. Blade surface pressure results obtained with the present DG flow solver are compared with those obtained using the TURNS flow solver (Refs. 12, 22, 30, 24) available at Boeing Mesa, which can be regarded as a prototype system using a more conventional CFD algorithm. The vortex persistence for the Caradonna-Tung rotor is illustrated by showing iso-contours of the rotary stagnation pressure loss both for a medium grid with adaption and a fine grid without adaption. Finally, concluding remarks are made.

2 CFD algorithm

2.1 Discontinuous Galerkin method

The DG flow solver is based on a discontinuous Galerkin finite element discretization of the unsteady Euler equations (Refs. 7, 8, 26).

Discontinuous Galerkin finite element methods use a discontinuous function space to approximate the exact solution of the Euler equations. A short introduction to these DG methods is provided by the lecture notes of a NATO special course on 'Higher Order Discretization Methods in CFD' (Ref. 7). One of the main advantages of the DG finite element method is its inherent ability to handle adaptivity strategies since the refining and unrefining of the grid is done without taking into account the continuity restrictions typical of conventional CFD methods (Refs. 26, 28).

2.2 Unique features

A unique feature of the present second-order accurate discontinuous Galerkin finite element method is that equations are solved not only for the mean flow field, but also for the flow field gradients. This results in a very compact scheme, because it is not necessary to reconstruct a flow field gradient, necessary to achieve second order accuracy, using data in neighbouring elements. The present finite element method has shock capturing capabilities and is easy to parallelize because there is limited communication between neighbouring elements. The local behaviour of the present finite element method is also beneficial for grid adaption, which is done using anisotropic grid refinement.

At this point it should be remarked that anisotropic element-by-element grid refinement is utilised in the present research to recover an isotropic grid from an anisotropic, initial grid. The anisotropy of the initial grid is often a concomitant feature of efficient, structured grids.

2.3 Standard features

Dynamic motions can be simulated using a rigidly translating-rotating reference frame connected to the configuration. This requires some modifications to the discontinuous Galerkin finite element method defined in an inertial frame, of which the most important one is the incorporation of the grid velocity in the flux formulation using an Arbitrary Lagrangian Eulerian (ALE) formulation. Using a Space-Time formulation the ALE DG method can be extended for simulation of arbitrarily moving multiple bodies, such as helicopter rotors in forward flight.

The discretization in time is based on an implicit time integration method. The use of an implicit time integration method is necessary, because there exists a very large discrepancy in time step

imposed by stability constraints and the necessary time step for sufficient accuracy due to very small grid sizes, for example close to sharp wing edges. The non-linear equations of the implicit time integration method are solved using a FAS multigrid method.

2.4 Vortex sensor and vortex grid adaption

Different quantities can be used to identify vortices within a flow, for example the total pressure loss (or rotary stagnation pressure loss for a rotor in hover, see section 3.5), the vorticity magnitude ($|\omega|$, where ω is the vorticity $\nabla \times \mathbf{u}$), and the helicity ($\mathbf{u} \cdot \omega$). Looking at topological properties of the flow in a vortex core the following vortex sensor was proposed (Ref. 11). For a three-dimensional flow the velocity gradient tensor $\nabla \mathbf{u} = \frac{\partial(u,v,w)}{\partial(x,y,z)}$ has three eigenvalues. In case two of these eigenvalues are complex, the flow can be characterized locally as a vortex flow. The magnitude of the imaginary part of these complex eigenvalues represents the so-called vortex strength.

In this paper the vortex sensor based on the total pressure loss or rotary stagnation pressure loss has been used to define a vortex grid adaption sensor. The general idea behind this vortex grid adaption sensor is that to minimize the numerical diffusion of the vorticity and numerical dissipation in a vortex the grid within the vortex should be as isotropic, as uniform and as refined as possible. For each computational direction the following vortex grid adaption sensor is defined. The sensor for computational direction i equals the total pressure loss (or rotary stagnation pressure loss) times h_i for elements with h_i larger than a specified value. Here h_i is the element width in computational direction i. For the other elements the vortex grid adaption sensor equals zero. All elements with a vortex grid adaption sensor not equal to zero are refined in the i-direction to obtain a more isotropic, uniform and refined grid in the vortex.

3 Extensions for rotor simulations

The extension of the DG flow solver algorithm developed for fixed wing aircraft to the simulation of rotor flows consists of a number of steps, which will be discussed in this section.

3.1 Blade motion definition

During forward flight a helicopter blade makes a complicated motion, consisting of a main rotor rotation, a pitching motion, a flapping motion and possibly a lead-lag motion. In addition the blade also experiences elastic deformation. The simulation of a helicopter rotor in forward flight therefore requires the definition of the blade motion.

The blade motion is generated using a sequence of coordinate system translations and rotations, each one defined relative to the previous one. For each blade in the computational domain the sequence of coordinate transformations is defined and in this way a completely general blade motion definition algorithm is obtained.

3.2 Grid deformation algorithm

In order to allow the blade motion it is necessary to locally deform the grid around the rotor blades. The calculation of the grid deformation is comparable with the grid generation problem and is subject to similar requirements, such as the prevention of grid folding, especially around sharp corners such as trailing edges.

After the calculation of the coordinate transformations for each rotor blade, the points on the blade surface are moved towards the new blade position, and the remaining part of the grid is deformed to accommodate the surface grid movement. This movement of the grid points is accomplished by solving a partial differential equation on a tetrahedral background mesh describing the grid motion (Ref. 15). The heuristic to prevent the folding of the smaller elements of the mesh (Ref. 15) is not necessary for the grids used in the present simulations. The resulting linear system is solved iteratively with a conjugate gradient method.

3.3 Boundary conditions for rotor in hover

An improved far field boundary conditions for hover simulations can be derived using one-dimensional helicopter momentum theory (Refs. 21, 23).

In this method the rotor is described as an actuator disc and the far field wake velocity is calculated using actuator disc theory. The wake velocity obtained from actuator disc theory induces a mass flux which must be balanced by an opposite mass flux through the inflow boundaries. This mass

flux is assumed to be uniformly distributed over sphere of radius r located at the center of the rotor disc. The thus obtained inflow velocity is added to the inflow boundary condition, resulting in an improved far-field boundary condition. In this analysis it is assumed that the flow field is incompressible and the helicopter rotor is approximated as an actuator disc with a constant loading. This hover boundary condition requires as input the rotor disc center and radius, the center of the rotor wake at the outflow boundary and a known thrust coefficient.

3.4 Rotor in hover as steady state problem

A helicopter rotor in hover can be considered as a steady state problem when the Euler equations are formulated in a reference frame rotating with the same angular velocity vector as the helicopter rotor. This requires less computational effort than the solution of the equivalent time-accurate problem.

When defining the rotor in hover condition as a steady state problem, i.e. by using a single rotating reference frame, an additional source term accounting for the Coriolis force is introduced into the Euler equations (Ref. 2).

3.5 Rotary stagnation pressure

If one considers the helicopter rotor in hover as a steady state problem by formulating the Euler equations in a reference frame rotating with the same angular velocity vector as the helicopter rotor, the total pressure is no longer uniform in space for an isentropic flow, but varies with the radial coordinate. Therefore, the total pressure loss cannot be used to identify the vortex location. In a rotating reference frame, however, an equivalent of the total pressure loss, being the rotary stagnation pressure loss, can be derived from the uniformity of rothalpy for isentropic flow in a similar manner as the total pressure loss is derived from the uniformity of enthalpy for isentropic flow in a fixed reference frame.

In a rotating reference frame the rothalpy is defined as

$$H_r = \frac{\gamma}{\gamma - 1}\frac{p}{\rho} + \frac{1}{2}\mathbf{u}\cdot\mathbf{u} - \mathbf{u}\cdot\mathbf{s}$$

Here p is the pressure, ρ the density, γ the ratio of specific heats, $\mathbf{u}$ the velocity vector and $\mathbf{s}$ the grid velocity vector. The rotary stagnation pressure loss equals

$$P_{rs} = 1 - \gamma p\left(1 + (\gamma - 1)\left(\frac{1}{2}\mathbf{u}\cdot\mathbf{u} - \mathbf{u}\cdot\mathbf{s}\right)\right)^{\frac{\gamma}{\gamma-1}}$$

Note that at infinity $P_{rs} = 0$ because the rotary stagnation pressure equals $1/\gamma$, the velocity vector equals zero and the pressure equals $1/\gamma$ at infinity for the present scaling (Ref. 26).

4 Accuracy and efficiency

As opposed to 'Chimera' or Overset grid techniques conservation of flux variables is easily accomplished in Arbitrary Lagrangian Eulerian methods since a single, time-varying grid is used. Combined with a discontinuous Galerkin discretization, ALE methods provide a powerful CFD technology for rotor wake analysis.

The distinguishing CFD key feature of the current algorithmic approach is the element-by-element anisotropic h-refinement capability of the DG algorithm. The DG algorithm allows this h-refinement on an element-by-element basis without any special algorithmic components for hanging edges and vertices. Conventional CFD algorithms cannot handle hanging edges and vertices without considering them as special cases. The present second-order accurate DG algorithm remains accurate without special consideration of hanging entities.

Standard multigrid acceleration techniques can be applied to achieve a computationally efficient algorithm, since the discontinuous Galerkin method allows explicit time integration schemes for steady state problems. The same multigrid algorithm can be used in an implicit time integration scheme for time-dependent problems. Moreover, since the discontinuous Galerkin method is extremely local, parallelization by grid partitioning requires minimal communication overhead and excellent speed-ups of 11.5 out of 14 are obtained on the NLR NEC SX-4/16 parallel vector super computer (Ref. 27). The present simulations are performed on the NLR NEC SX-5/8 parallel vector super computer.

5 Transonic unsteady rotor Navier-Stokes(TURNS)

An important point in the Boeing classification of stages in the development of CFD capabilities is the comparison between prototype systems using various approaches. In the present research the results obtained with the DG flow solver are compared with those obtained using the TURNS flow solver (Refs. 12, 22, 30, 24). TURNS stands for Transonic Unsteady Rotor Navier-Stokes, and is based on a finite difference, upwind numerical algorithm. Unlike the DG flow solver, the TURNS flow solver has been developed specifically for helicopter rotor applications. In TURNS an upwind-biased flux-difference scheme (originally suggested by Roe, later extended to three-dimensional flows by Vatsa) is used to evaluate the inviscid fluxes. Second- or third-order accuracy has been established by using the Van Leer MUSCL approach using flux limiters in order to be total variation diminishing (TVD). Standard second-order central differencing is used for the discretization of the viscous flux terms. The LU-SGS method which is a direct modification of the approximate lower-diagonal-upper (LDU) factorization to the unfactored implicit matrix is used as the time-marching procedure. A modified finite-volume method is used to calculate the metrics. The space metrics are evaluated at grid points instead of cell interfaces in order to be compatible with the finite difference numerical scheme. The time metrics are evaluated in the same manner as in a finite difference scheme. For more details of the TURNS algorithm see (Ref. 22).

6 Test cases

Three test case are considered. The vortex grid adaption sensor has been tested on the ONERA M6 wing as a first test case. The simulations are performed using an angle of attack α of 6°, and a freestream Mach number M_∞ of 0.4.

In a second test case the rotor flow simulation capabilities of the DG flow solver are tested against the standard Caradonna-Tung experiment.

The Caradonna-Tung experiment was conducted at NASA Ames and consists of a two-bladed helicopter rotor in hover (Ref. 6). The rotor employs two cantilever-mounted, manually adjustable blades. These blades have a NACA-0012 profile and are untwisted and untapered. The blade aspect ratio of the Caradonna-Tung rotor is 6. At five radial sections, viz. z/R =0.5, 0.68, 0.8, 0.89 and 0.96, pressure transducers were located. The experiments were performed for collective pitch settings of 0°, 2°, 5°, 8° and 12°, and angular frequencies Ω ranging from 650 to 2540 rpm. For the case discussed in the present paper, a collective pitch setting of 12°, an angular frequency of 1750 rpm and a tip Mach number M_{tip} of 0.61 were used. Here the tip Mach number is defined as $M_{tip} = \Omega R_{tip}/a_\infty$, with R_{tip} the rotor blade tip radius and a_∞ the free stream speed of sound.

The third test case involves the two-bladed OLS helicopter rotor in forward flight for BVI conditions and is subject of ongoing research.

7 ONERA M6 results

Three simulations are performed, i.e. a medium grid simulation without adaption, a medium grid simulation with adaption and a fine grid simulation. The medium grid consists of 55,040 elements, and the fine grid consists of 440,320 elements.

7.1 Fine grid

The convergence histories of the residuals on the fine grid are presented in Figs. 1(a)-(d). Fig. 1(a) presents two norms of residuals of the five equations for the element averages of the state vector (of the Euler equations). Fig. 1(b) presents two norms of residuals of the five equations for the element ξ-gradients of the state vector. Figs. 1(c) and 1(d) present the corresponding norms of the residuals in the η- and ζ-gradients, respectively (ξ, η and ζ are the local coordinates per element). Simple addition learns that the present second-order accurate DG algorithm consists of 20 non-linear, algebraic equations per element. Fig. 1 shows that all residuals do converge which is a key requirement if one wishes to inspect the vorticity (state vector gradients).

Fig. 2 shows an iso-contour of the total pressure loss on the fine grid. Note that the contour extends towards the outflow boundary (12 wing spans behind the wing).

This fine grid CFD solution shows the DG capability to accurately simulate the persistence of the trailing vorticity, provided all the ξ-, η- and ζ-gradients of the CFD solution are sufficiently converged. Note that this fine-grid simulation consists of 440,320 elements with 20 degrees of freedom per element resulting in a total of 8,806,400 degrees of freedom. The main advantage of the DG approach is that the same vortex persistence can also be obtained on a medium grid with adaption.

7.2 Grid adaption

In the simulation of the medium grid with adaption the grid is adapted twice. During each adaption step the number of elements is increased by approximately 10 percent, so that the resulting grids consist of 55,040 and 68,944 elements. The results of the relative vortex strength, i.e. the vortex strength divided by the vortex strength at one wing span behind the wing, is shown in Fig. 3. In this figure both the relative vortex strength based on the total pressure loss and on the vortex strength (see section 2.4) are shown. The wake region in the unadapted grid is characterized by anisotropic elements in the flow direction. Therefore elements are automatically adapted in the flow direction. Fig. 3 shows that for the twice adapted grid, which has 15.66 percent of the elements of the fine grid, the relative vortex strength based on both the total pressure loss and the vortex strength is

equal to that obtained with the fine grid. Note, furthermore, that the decay of the vortex is much smaller in terms of total pressure loss than in terms of vortex strength, which suggests that a vortex grid adaption sensor using the total pressure loss (or rotary stagnation pressure loss for a rotor in hover) instead of the vortex strength is more appropriate to minimize the grid anisotropy in the vortex.

This application of adaptivity to a vortex persistence problem demonstrates that the second requirement for CFD algorithms, defined in section 1.3, can be satisfied by a second-order DG algorithm (1.5 revolutions is approximately equal to 5 diameters, which is less than 10 wing spans).

7.3 Need for extension to Navier-Stokes

It should be noted that for this specific simulation the grid has only been adapted in the wake using the above described vortex grid adaption sensor. No adaption near the wing has been performed, since this would only result in an unbounded increase of the vortex resolution. This unboundedness of the Euler solution in vortex cores near the tip of a blade is a direct consequence of the fact that the Euler equations are strictly non-diffusive. Total lack of diffusion results in unboundedness of the vorticity under grid refinement. Introduction of Navier-Stokes equations with a finite diffusivity will eliminate this unboundedness, and will allow grid refinement until all finite gradients are well resolved.

8 Caradonna-Tung rotor in hover

8.1 Caradonna-Tung OH-grid

At NLR a single-block grid of one half of the computational domain containing one blade of the Caradonna-Tung helicopter rotor was available. For this grid the rotor blade is in the center of the computational domain and connected to an axis where a slip flow boundary condition is applied. The grid has an O-topology around the blade and a H-topology parallel with the blade. The blade tip was square with a finite thickness in the experiment, but is reduced to zero thickness in the last cell in order to facilitate the grid generation process. For a figure of this grid, see Ref. 16, Bild 21, OH-Netz für einen zweiblättrigen Rotor in Schwebeflug.

Simulations on this grid showed that, although giving the correct pressure distribution on the rotor blade and the correct thrust coefficient, the grid is insufficient to correctly capture the tip vortex over a distance of one-and-a-half revolutions.

The insufficiency of this single block OH-grid pertains in particular to the grid quality near the blade tip; to allow for a quantum jump in grid quality the blade tip geometry has been complemented with a cap (by revolving the NACA0012 tip profile around its x-axis).

8.2 Caradonna-Tung multi-block grid

For the new grid around the Caradonna-Tung helicopter rotor the good properties of the ONERA M6 grid used to assess the vortex capturing capabilities of the DG flow solver have been transferred to the rotor case. The grid point distribution on the rotor blade is taken to resemble the grid point distribution on the rotor blade in the existing, OH-type Caradonna-Tung grid as close as possible. The multi-block topology around the blade is illustrated in Figs. 4(a) and 4(b). Since the tip vortex moves both inward and downward (see for example Figure 9 of Ref. 10), special attention was given to this region of the grid. In this region a grid with as uniform as possible elements has been generated, also in the circumferential direction, see Figs. 5(b) and 6(b). The control over the location of the grid points below the rotor blade is facilitated by introducing an additional set of blocks below the rotor blade (compare Figs. 5(a) and 6(a)). Since the tip vortex moves downward more elements are located below the rotor than above the rotor. Near the outflow boundary the aspect ratio of the elements in the flow direction is increased to obtain a large amount of numerical dissipation resulting in a destruction of the vortex so that no interaction between the vortex and the outflow boundary condition is expected to occur, see Fig. 6(a).

The resulting multi-block grid of one half of the computational domain consists of 55 blocks, with

a total of 726,784 elements and 823,599 grid points (fine grid). However, simulations may also be performed on a one-time coarsened grid, i.e. with a total of 90,848 elements (medium grid).

8.3 Caradonna-Tung CH-grid

The grid used by the TURNS flow solver has a C-topology around the blade and a H-topology parallel with the plane of the blade. The grid used has 299 grid points in the wraparound C-direction, 71 points in the spanwise direction and 61 points in the normal direction. The total number of grid points in this grid equals $299 \times 71 \times 61 = 1{,}294{,}969$. The grid is initially generated using a hyperbolic grid generator and is then curved in the azimuth direction to provide for periodicity near the zero and 180 degrees azimuth positions. The grid extends one rotor radius beyond the blade tip in the spanwise direction, and also one rotor diameter above and below the plane of the rotor.

8.4 Caradonna-Tung surface pressure results

The flow field around the Caradonna-Tung helicopter rotor using a collective pitch setting of 12° and a tip Mach number M_{tip} of 0.61 has been simulated by using the DG solver on the medium grid with grid adaption and on the fine grid without grid adaption. The DG results are compared with those obtained using the TURNS flow solver on the CH-grid. Note that the medium grid originally contains 90,848 elements, that the fine grid contains 726,784 elements and that the TURNS grid contains 1,261,600 cells. After adaption the medium grid contains 135,280 elements.

In Fig. 7 the -C_p-distribution at five radial stations obtained by the simulations is compared with the experimental data (Ref. 6). The agreement between the DG flow solver simulations and the experimental data is generally good. The pressure peak at the lower side of the rotor blade is, however, resolved better on the fine grid. The agreement between the DG flow solver results and the TURNS flow solver results on the upper side of the rotor is fair; the DG flow solver resolves the pressure peak better. At the lower side the TURNS results have a $-C_p$-value higher than the experimental value, which does not seem to be consistent with earlier results (Ref. 22). The DG flow solver results coincide very well with the experimental pressure data at the lower side.

8.5 Vortex persistence for Caradonna-Tung rotor

Figs. 8(a) and 8(b) present the rotary stagnation pressure loss (defined in section 3.5) for different radial cross-sections, i.e. 20, 50, 90 and 140 $^\circ$ behind blade 1, for both the medium grid with adaption and the fine grid without adaption. Comparing the DG results with and without adaption at the 140° azimuth position behind blade 1 shows that adaption improves the vortex signature in terms of rotary stagnation pressure loss.

Fig. 10 shows two iso-contours of the rotary stagnation pressure for the medium grid with adaption and the fine grid without adaption. From these figures it is clear that the DG flow solver is able to capture the tip vortex over a distance of one-and-a-half revolution. For a value of the rotary stagnation pressure loss of 0.0119 the fine grid solution is slightly more concentrated and shows a longer vortex. The grid adaption, however, results in an increase of the vortex length defined by the rotary stagnation pressure loss contour of 0.02. Thus, at this higher value, grid adaption results in an increased vortex resolution (compare Fig. 10(a) and 10(b) for $P_{rs} = 0.02$).

The local behavior of the grid adaption is presented in Fig. 9. Here, rotor blade 1, the periodic plane at $z = 0$ and the plane at $x = -3.6$ are shown. Clearly visible are the places where the vortex intersects these planes. At those positions one can see that the grid has been adapted to obtain a grid as isotropic and as uniform as possible in the vortex.

Fig. 11 presents a blow-up of the DG solution given in Fig. 10(b) and shows the iso-contours near the tip on the fine grid obtained using four different values of the rotary stagnation pressure loss. Note that the complete iso-contour of $P_{rs} = 0.02$ has been shown in Fig. 10(b). Increasing the value of the rotary stagnation pressure loss shows that the tip vortex originates at the upper side of the tip cap, and not at the intersection point of the tip cap and the wing trailing edge.

9 Discussion

In this paper an innovative CFD algorithm for the simulation of rotor wake vortices has been presented. This algorithm is a DG finite element algorithm based on an ALE formulation in conjunction with anisotropic grid refinement of hexahedral elements. In section 1.3 the basic requirements for this CFD algorithm to be able to simulate helicopter rotor flows have been identified.

Features of the presented discontinuous Galerkin approach are:

(i) the vorticity is carried as an independent flow variable; it is implicitly related to the ξ-, η- and ζ-gradients of the state vector (15 variables per element),

(ii) the algorithm allows degenerate, high-aspect ratio elements near leading and trailing edges of blades for efficiency,

(iii) the algorithm has an extremely compact stencil, and as a result possesses an inherent ability to handle adaptive strategies since the refining and derefining of the elements (grid) is done without any need to consider special continuity requirements typical of conventional CFD methods,

(iv) the algorithm has an excellent parallization potential because the communication between neighboring elements is strictly limited to the evaluation of the basis functions at common faces, and will therefore be well suited for parallel computing platforms,

(v) extension of the DG algorithm from Euler to Navier-Stokes equations is feasible, e.g. see Ref. 1 for an analysis in two dimensions, without compromising items (i) through (iv) above,

(vi) the algorithm is well suited for vortex persistence problems; in sections 7 and 8 it has been shown that the DG flow solver is able to capture the tip vortex over a distance of at least 12 wing spans for the ONERA M6 test case, and over a distance of at least one-and-a-half revolutions for the Caradonna-Tung helicopter rotor test case, if the multigrid iterations are continued until the residuals are sufficiently converged,

(vii) metrics for the DG methods relative computational efficiency in comparison with more conventional CFD algorithms have not been developed as yet; to this end one would need to identify a common vortex persistence problem and compare the required computational resources at the Navier-Stokes level for equal vortex signatures at large distances (either in terms of spanwise length or in terms of revolutions).

10 Concluding remarks

The algorithmic research of this paper falls in the proliferation stage of CFD development. Attention is focussed on basic requirements for CFD algorithms. The most important issue explored in the present paper is the ability of the discontinuous Galerkin finite element approach to capture tip vortices over large distances. The conclusion is that the present DG algorithm can capture vortices over large distances provided the multigrid iterations are continued until all the residuals of the 20 non-linear, algebraic equations per finite element are sufficiently converged. For the ONERA M6 and Caradonna-Tung test cases it is found that the convergence tolerance required for the accurate capture of trailing vortices is significantly tighter than the equivalent convergence tolerance needed to capture transonic shock waves; i.e. transonic shock waves are easy to capture relative to the far field signature of trailing vortices.

Comparison of the present DG results with the results of the more conventional, TURNS algorithm shows that the present DG approach yields the same or better agreement between CFD and experimental data in terms of surface pressures on a rotor blade in hover.

To assess the relative computational efficiency of the DG approach (with grid adaption) in comparison with more conventional CFD algorithms one would need to identify a common vortex persistence problem and compare the required computational resources at the Navier-Stokes level for equal vortex signatures at large distances. This assessment of relative computational complexity of DG algorithms with grid adaption for stiff problems remains as a challenge for future projects. Provided such an assessment of the computational complexity of the proposed algorithm can be concluded successfully, one can conclude that the proposed combination of the standard ALE formulation with the unconventional DG finite-element method (including grid adaption) can meet the basic requirements for CFD algorithms that need to be satisfied if one wishes to establish standard and reliable CFD tools for BVI noise.

Acknowledgements

The authors would like to acknowledge the support of the Royal Netherlands Air Force (RNLAF, contract number N98/19), The Boeing Company, Mesa and NLR; we also like to thank S.P. Spekreijse and H.A. Sytsma of the NLR for making the Caradonna-Tung grid, and J.J.W. van der Vegt of the University of Twente, Enschede, The Netherlands for his contributions to the DG flow solver algorithm.

References

1. ATKINS, H.L. AND C.W. SHU 1999 Analysis of the Discontinuous Galerkin method to the Diffusion Operator. *AIAA* **99-3306**.
2. BONIFACE, J.C. AND J. SIDES 1993 Numerical simulation of steady and unsteady euler flows around multibladed helicopter rotors. *Paper presented at 19^{th} European Rotorcraft Forum* Cernobbio, Como, Italy.
3. BONIFACE, J.CH. AND K. PAHLKE 1996 Calculations of multibladed rotors in forward flight using 3D Euler methods of DLR and ONERA. *Paper presented at 22^{nd} European Rotorcraft Forum* Brighton, United Kingdom.
4. BOTTASSO, C.L. AND M.S. SHEPHARD 1997 Parallel adaptive finite element Euler flow solver for rotary wing aerodynamics. *AIAA Journal* **35**, 937–944.
5. BOXWELL, D.A., SCHMITZ, F.H., SPLETTSTOESSER, W.R. AND K.J. SCHULTZ 1987 Helicopter model rotor-blade vortex interaction impulsive noise: Scalability and parametric variations. *Journal of American Helicopter Society* **32**, 3–12.
6. CARADONNA, F.X. AND C. TUNG 1981 Experimental and Analytical Studies of a Model Helicopter Rotor in Hover. *NASA Technical Memorandum* **81232**.
7. COCKBURN, B. 1999 Discontinuous Galerkin methods for convection-dominated problems. In *High-order methods for computational physics*, T. Barth and H. Deconinck (Eds.), LNCSE 9, Springer Verlag.
8. COCKBURN, B., KARNIADAKIS, G. AND C.-W. SHU 1999 An overview of the development of discontinuous Galerkin methods. *Lecture Notes in Computational Science and Engineering* **11**, Springer Verlag.
9. COSNER, R.R. August 1999 Overview of Computational Fluid Dynamics at The Boeing Company. *Private communication*.
10. CONLISK, A.T. 1999 The Fluid Dynamics of Rotor Wakes: Theory, Computation and Experiment. *AIAA* **99-3421**.
11. DINDAR, M. 1998 An adaptive finite element procedure for rotorcraft aerodynamics and aeroelasticity. Rensselaer Polytechnic Institute, Troy, New York.
12. DUQUE, E.P.N. AND G.R. SRINIVASAN 1992 Numerical simulations of a hovering rotor using embedded grids. *Paper presented at American Helicopter Society 48^{th} Annual Forum* Washington DC, USA.
13. DUQUE, E.P.N., STRAWN, R.C., AHMAD, J. AND R. BISWAS 1996 An overset grid Navier-Stokes Kirchhoff-surface method for rotorcraft aeroacoustic predictions. *AIAA* **96-0152**.

14. LORBER, P.F. October 1991 Aerodynamic results of a pressure-instrumented model rotor test at DNW. *Journal of the American Helicopter Society*, 66–76.

15. MASUD, A. AND T.J.R. HUGHES 1997 A space-time Galerkin/least squares finite element formulation of the Navier-Stokes equations for moving domain problems. *Comp. Meth. In Applied Mech. and Engrg.* **146**, 91–126.

16. PAHLKE, K. 1999 Berechnung von Strömungsfeldern um Hubschrauberrotoren im Vorwärtsflug durch die Lösung der Euler-Gleichungen. *Forschungsbericht* **1999-22**, Deutsches Zentrum für Luft- und Raumfahrt e. V.

17. RADDATZ, J. AND K. PAHLKE 1995 Calculations of Multibladed Rotors in Hover using 3D Euler Methods of DLR and ONERA. *21^{st} European Rotorcraft Forum* Paper II-6, Saint Petersburg, Russia.

18. SHOCKEY, G.A., WILLIAMSON, J.W. AND C.R. COX May 1976 Helicopter aerodynamics and structural loads survey *32^{nd} Annual Forum of the American Helicopter Society*, Washington, DC, USA.

19. SPLETTSTOESSER, W.R., NIESL, G., CENEDESE, F., NITTI, F. AND D.G. PAPNIKAS April 1995 Experimental results of the European HELINOISE aeroacoustic rotor test. *Journal of the American Helicopter Society*, 3–14.

20. SPLETTSTOESSER, W.R., KUBE, R., WAGNER, W., SEELHORST, U., BOUTIER, A., MICHELI, F., MERCKER, E. AND K. PENGEL January 1997 Key results from a higher harmonic control aeroacoustic rotor test (HART). *Journal of the American Helicopter Society*, 58–78.

21. SRINIVASAN, G.R., RAGHAVAN, V. AND E.P.N. DUQUE 1991 Flowfield analysis of modern helicopter rotors in hover by Navier-Stokes method. *Paper presented at the International Technical Specialists Meeting on Rotorcraft Acoustics and Rotor Fluid Dynamics* Philadelphia, PA, USA.

22. SRINIVASAN, G.R., BAEDER, J.D., OBAYASHI, S. AND W.J. MCCROSKEY 1992 Flowfield of a lifting rotor in hover: A Navier-Stokes simulation. *AIAA Journal*, **30**, 2371–2378.

23. STRAWN, R.C. AND T.J. BARTH 1993 A finite volume Euler solver for computing rotary-wing aerodynamics on unstructured meshes. *Journal of the American Helicopter Society*, 61–67.

24. STRAWN, R.C., BISWAS, R. AND A.S. LYRINTZIS 1996 Helicopter noise predictions using Kirchhoff methods. *Journal of Computational Acoustics* **4**, 321–339.

25. TUNG, C., GALLMAN, J.M., KUBE, R., WAGNER, W., VAN DER WALL, B., BROOKS, T.F., BURLEY, C.L., BOYD JR., D.D., RAHIER, G. AND P. BEAUMIER 1995 Prediction and measurement of blade-vortex interaction loading. *Proceedings CEAS/AIAA* **95-051**, 365–376.

26. VAN DER VEGT, J.J.W. AND H. VAN DER VEN 1998 Discontinuous Galerkin finite element method with anisotropic local grid refinement for inviscid compressible flow. *J. Comput. Phys.* **140**, 1–32.

27. VAN DER VEN, H. AND J.J.W. VAN DER VEGT 1997 Experiences with advanced CFD algoritms on NEC SX-4, In *Parallel Processing VECPAR '96*, Palma and Dongarra (Eds.), Lect. Notes in Computer Science, Springer Verlag.

28. VAN DER VEN, H. AND J.J.W. VAN DER VEGT 1999 Accuracy, Resolution, and Computational Complexity of a Discontinuous Galerkin Finite Element Method. *Lecture Notes in Computational Science and Engineering* **11**, Springer Verlag.

29. WEBSTER, B.E., SHEPHARD, M.S., RUSAK, Z. AND J.E. FLAHERY 1994 Automated adaptive time-discontinuous finite element method for unsteady compressible airfoil aerodynamics. *AIAA Journal* **32**, 748–757.

30. WISSINK, A.M., LYRINTZIS, A.S., STRAWN, R.C., OLIKER, L. AND R. BISWAS 1996 Efficient helicopter aerodynamic and aeroacoustic predictions on parallel computers. *AIAA* **96-0153**.

31. YU, Y.H., TUNG, C., GALLMAN, J., SCHULTZ, K.J., VAN DER WALL, B., SPIEGEL, P. AND B. MICHEA 1995 Aerodynamics and acoustics of rotor blade-vortex interactions. *Journal of Aircraft* **32**, 970–977.

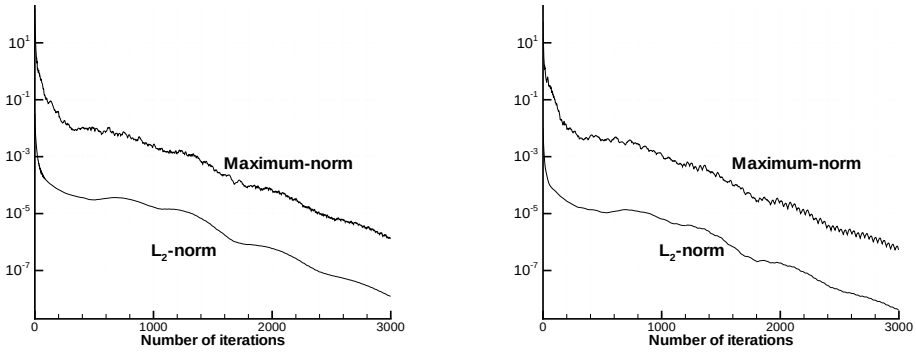

(a) mean (b) ξ-gradient

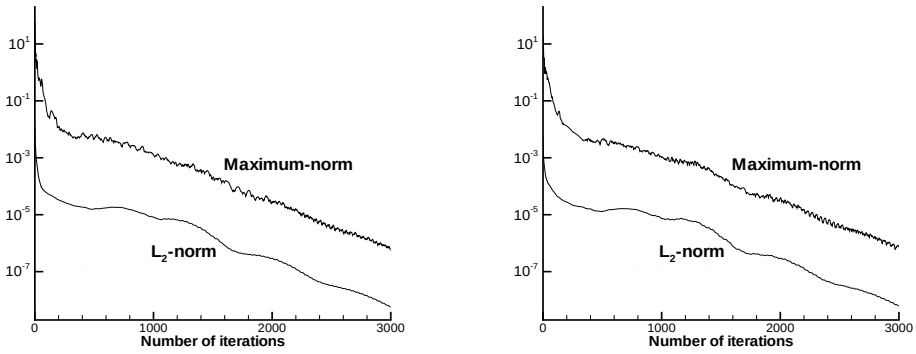

(c) η-gradient (d) ζ-gradient

Fig. 1 Convergence of the residuals for the ONERA M6 simulation on the fine grid (440,320 elements) ($\alpha = 6°$ and $M_\infty = 0.4$).

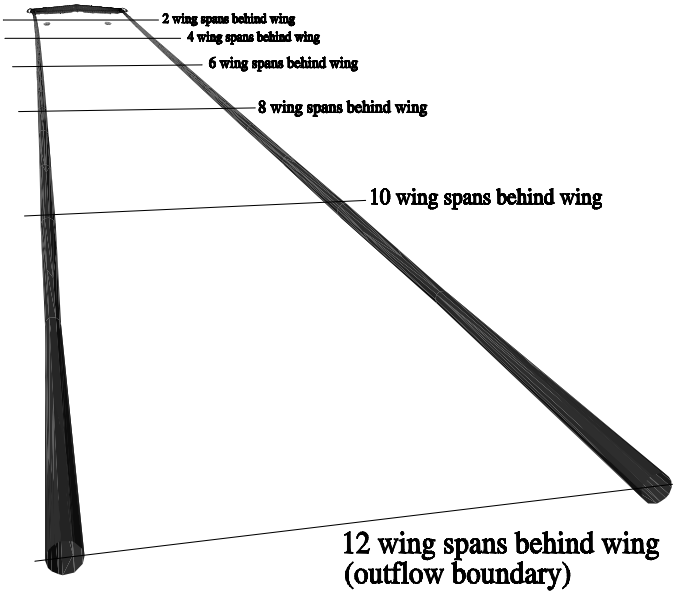

Fig. 2 Iso-contour of the total pressure loss (0.01) for the ONERA M6 simulation on the fine grid (440,320 elements) ($\alpha = 6°$ and $M_\infty = 0.4$), demonstrating DG capability to accurately simulate the persistence of the trailing vorticity.

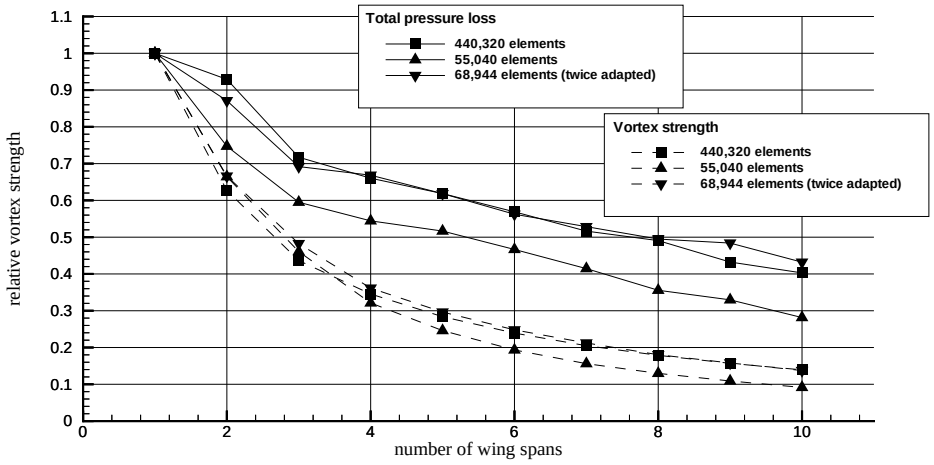

Fig. 3 The relative vortex strength, i.e. vortex strength/vortex strength at one wing span, for the ONERA M6 wing ($\alpha = 6°$ and $M_\infty = 0.4$). Both the relative vortex strength based on the total pressure loss and the vortex strength are shown.

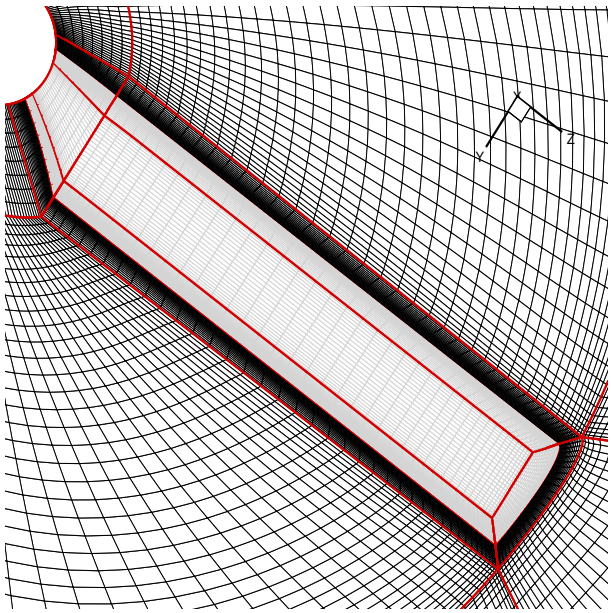

(a)

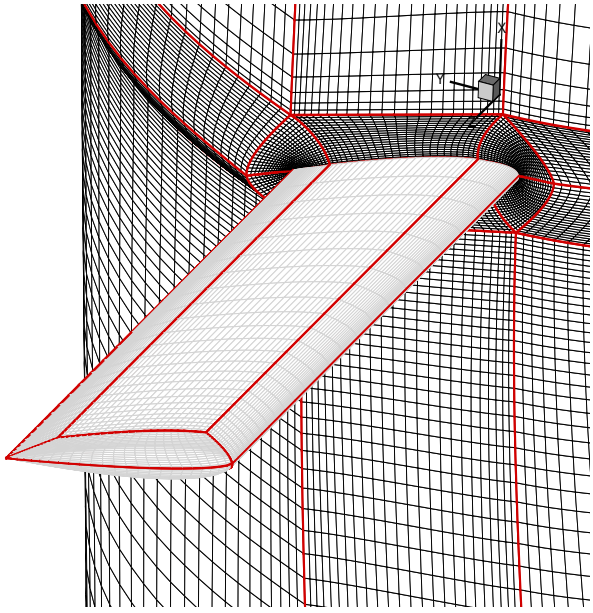

(b)

Fig. 4 The Caradonna-Tung grid near the blade (726,784 elements): (a) the blade and the plane trough the leading edge, trailing edge and blade tip, (b) the blade and a grid plane perpendicular to the blade. The rotor blade is coloured grey. The block boundaries are coloured red.

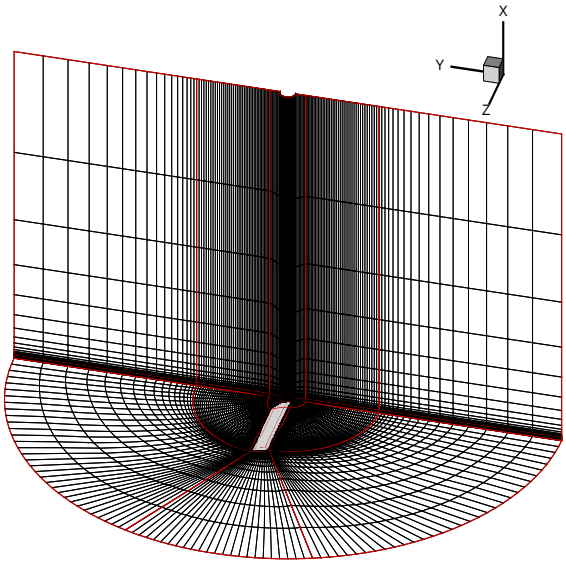

(a)

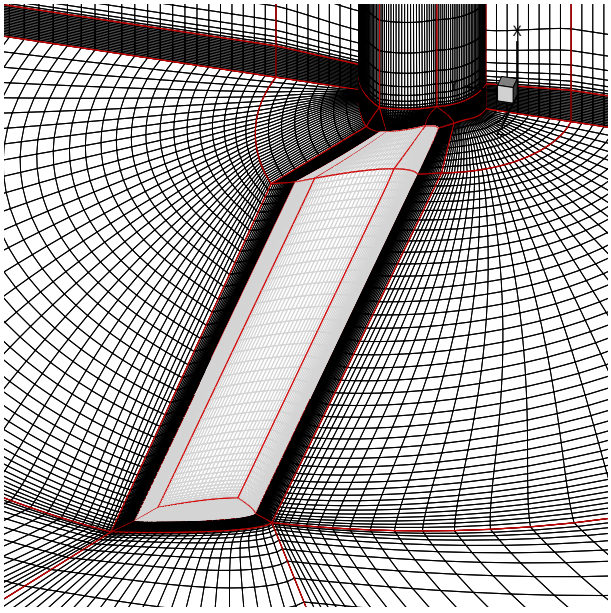

(b)

Fig. 5 The upper part of the Caradonna-Tung grid (726,784 elements): (a) the complete grid, (b) detail near the rotor blade. The rotor blade is coloured grey. The block boundaries are coloured red.

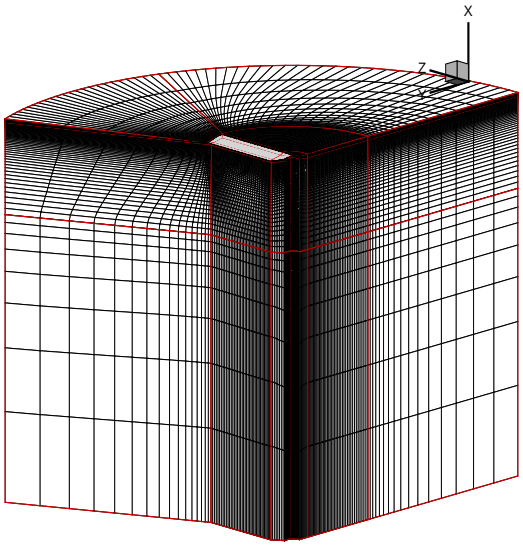

(a)

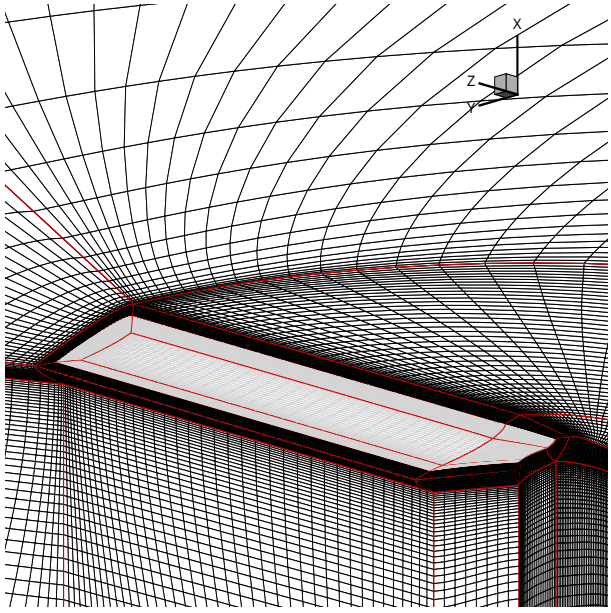

(b)

Fig. 6 The lower part of the Caradonna-Tung grid (726,784 elements): (a) the complete grid, (b) detail near the rotor blade. The rotor blade is coloured grey. The block boundaries are coloured red.

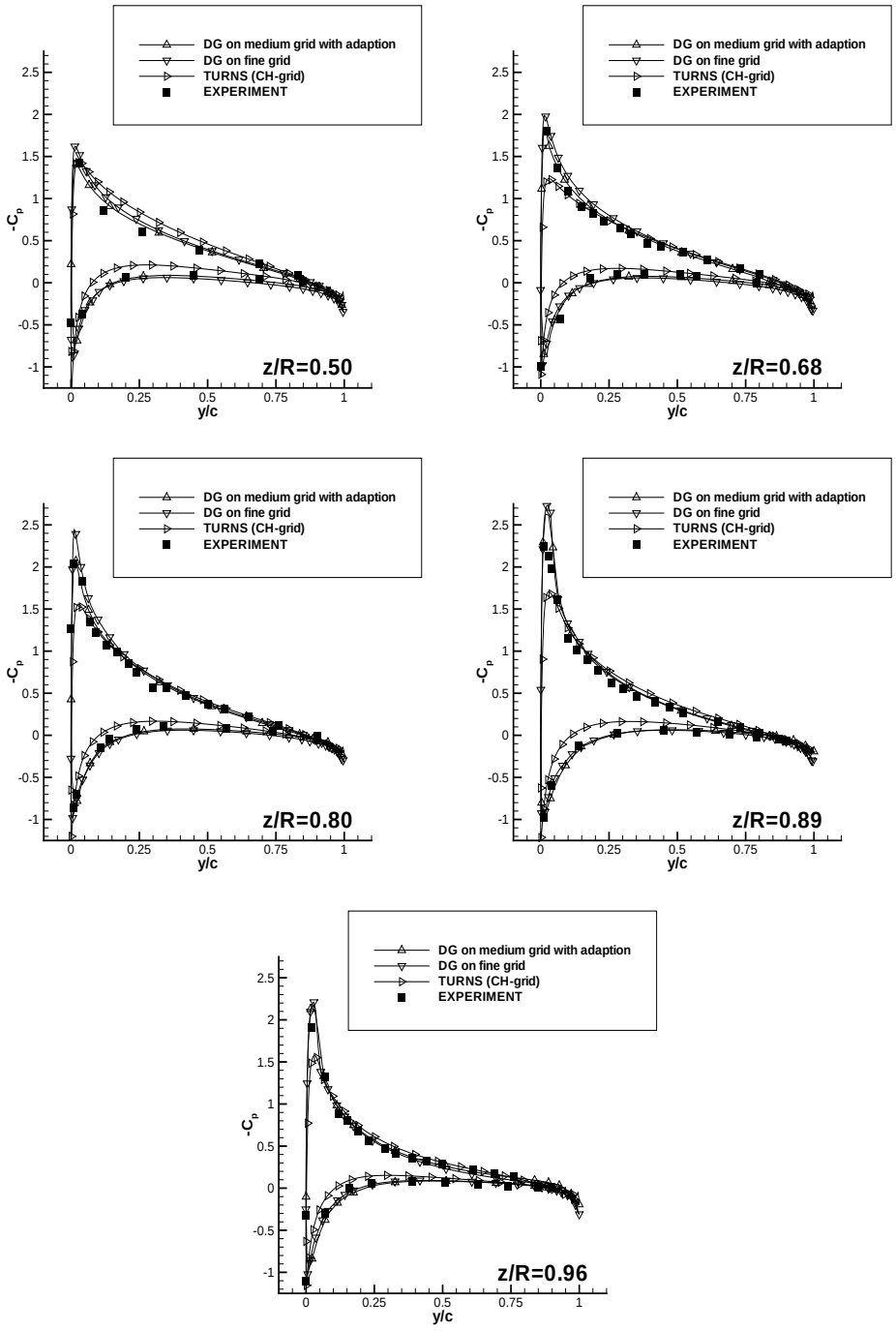

Fig. 7 Comparison of -C_p-distribution for the Caradonna-Tung helicopter rotor in hover (collective pitch: 12°, $M_{tip} = 0.61$, $Re = 2.7 \cdot 10^6$): C_T=0.0094 on the fine grid.

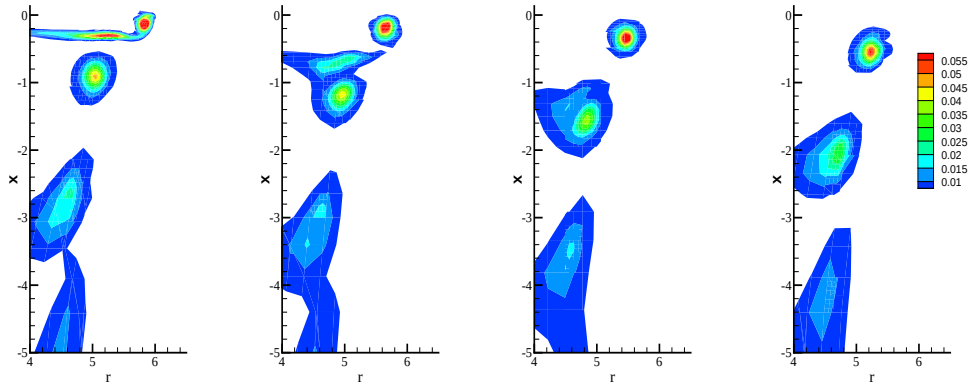

20° behind blade 1 50° behind blade 1 90° behind blade 1 140° behind blade 1

(a) medium adapted grid (135,280 elements)

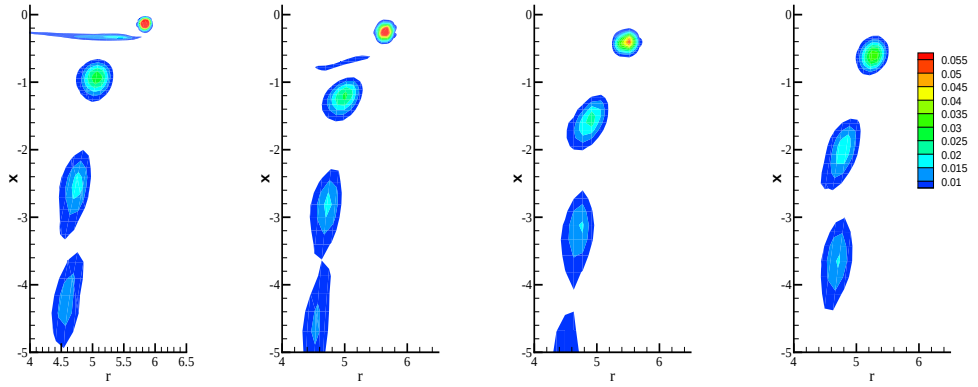

20° behind blade 1 50° behind blade 1 90° behind blade 1 140° behind blade 1

(b) fine grid (726,784 elements)

Fig. 8 Rotary stagnation pressure loss contours at different radial cross-section for the Caradonna-Tung helicopter rotor in hover on the medium adapted grid (a) and on the fine grid (b) (collective pitch: 12°, $M_{tip} = 0.61$).

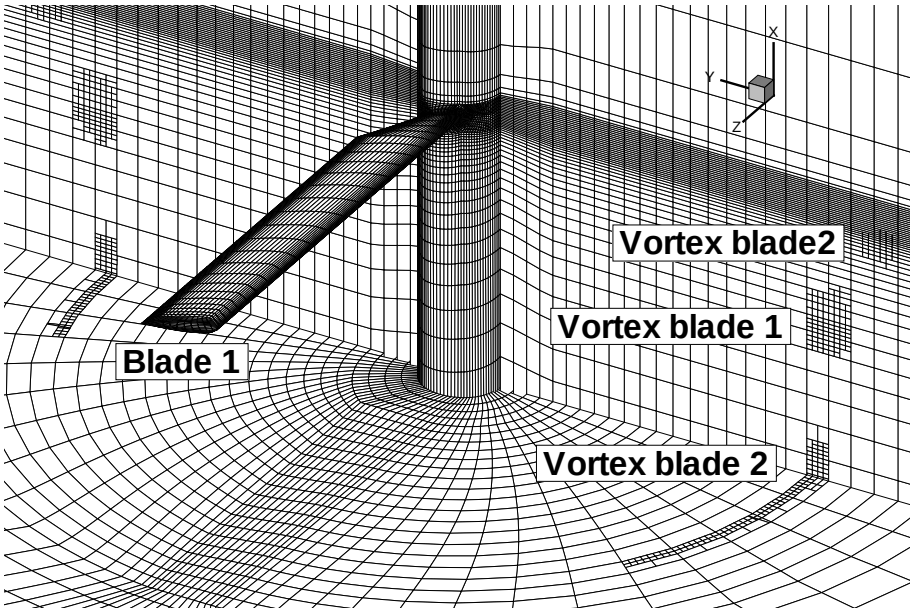

Fig. 9 The adapted Caradonna-Tung grid (135,280 elements). Shown are the periodic plane at z=0 and the plane at x=-3.6.

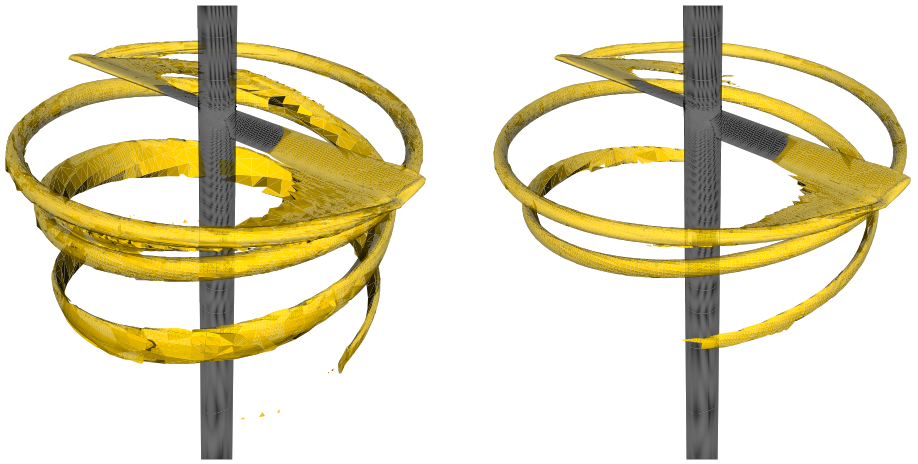

$P_{rs} = 0.0119$ $P_{rs} = 0.02$

(a) medium adapted grid (135,280 elements)

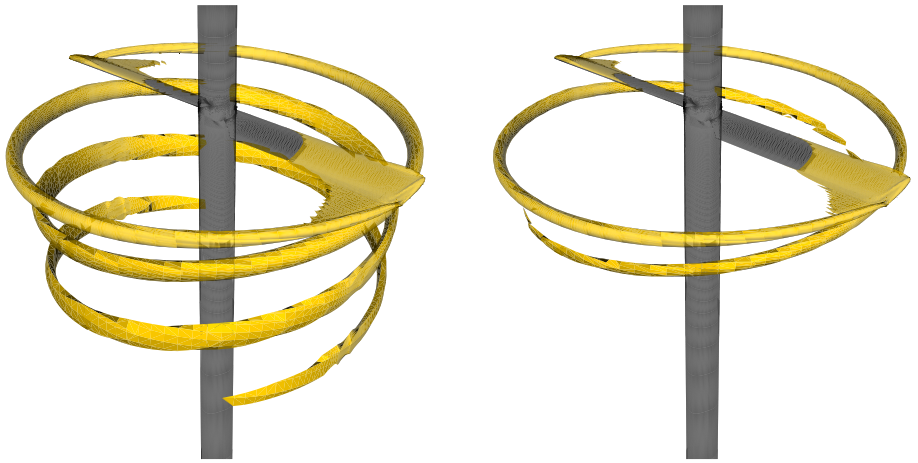

$P_{rs} = 0.0119$ $P_{rs} = 0.02$

(b) fine grid (726,784 elements)

Fig. 10 Iso-contour of the rotary stagnation pressure loss for the Caradonna-Tung helicopter rotor in hover on the medium adapted grid (a) and on the fine grid (b) (collective pitch: 12°, $M_{tip} = 0.61$).

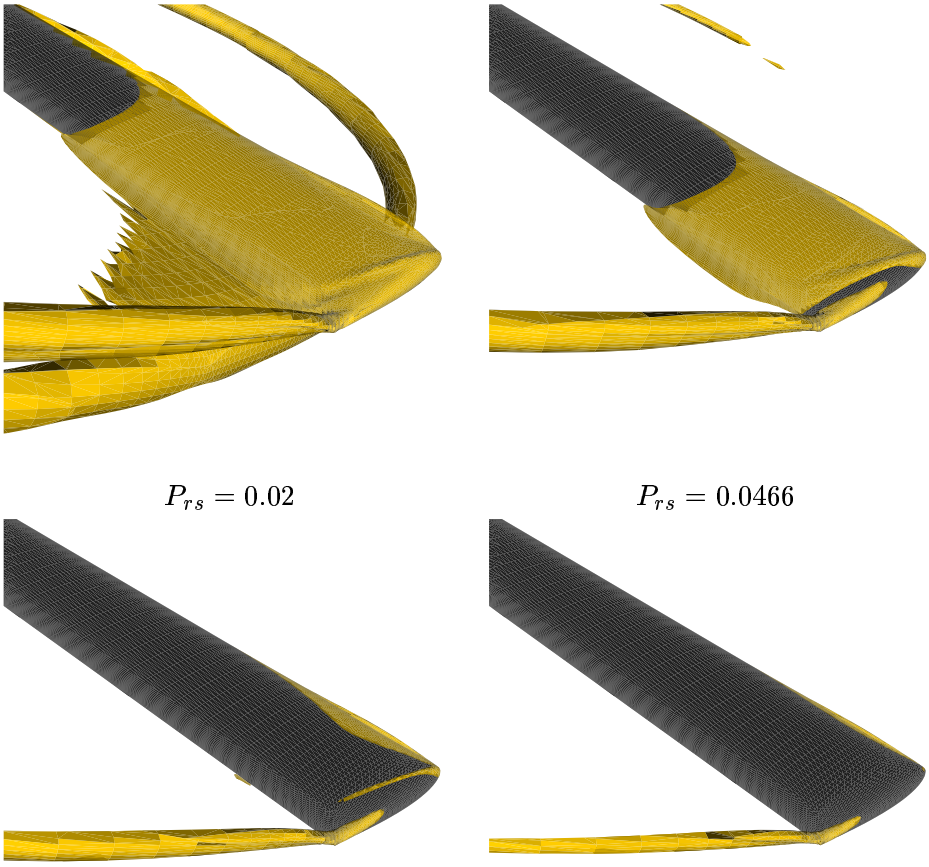

$P_{rs} = 0.02$ $P_{rs} = 0.0466$

$P_{rs} = 0.0733$ $P_{rs} = 0.1$

fine grid (726,784 elements)

Fig. 11 Iso-contour of the rotary stagnation pressure loss near the tip for the Caradonna-Tung helicopter rotor in hover on the fine grid. (collective pitch: 12°, $M_{tip} = 0.61$).